COMPUTATIONAL SCIENCE&DISCOVERY

Multi-scale continuum modeling of biological processes: from molecular electro-diffusion to sub-cellular signaling transduction

Y Cheng[1], P Kekenes-Huskey[2], J E Hake[1], M J Holst[3], J A McCammon[2] and A P Michailova[1]

[1] Department of Bioengineering, University of California, San Diego, La Jolla, CA 92093, USA
[2] Department of Pharmacology, University of California, San Diego, La Jolla, CA 92093, USA
[3] Departments of Mathematics and Physics, University of California, San Diego, La Jolla, CA 92093, USA
E-mail: yuhuic@gmail.com

Received 30 August 2011, in final form 9 February 2012
Published xxx
Computational Science & Discovery **12** (2012) 000000 (14pp)
doi:10.1088/1749-4699/12/1/000000

Abstract. This paper presents a brief review of multi-scale modeling at the molecular to cellular scale, with new results for heart muscle cells. A finite element-based simulation package (SMOL) was used to investigate the signaling transduction at molecular and sub-cellular scales (http://mccammon.ucsd.edu/smol/, http://FETK.org) by numerical solution of the time-dependent Smoluchowski equations and a reaction-diffusion system. At the molecular scale, SMOL has yielded experimentally validated estimates of the diffusion-limited association rates for the binding of acetylcholine to mouse acetylcholinesterase using crystallographic structural data. The predicted rate constants exhibit increasingly delayed steady-state times with increasing ionic strength and demonstrate the role of an enzyme's electrostatic potential in influencing ligand binding. At the sub-cellular scale, an extension of SMOL solves a nonlinear, reaction-diffusion system describing Ca^{2+} ligand buffering and diffusion in experimentally derived rodent ventricular myocyte geometries. Results reveal the important role of mobile and stationary Ca^{2+} buffers, including Ca^{2+} indicator dye. We found that alterations in Ca^{2+}-binding and dissociation rates of troponin C (TnC) and total TnC concentration modulate sub-cellular Ca^{2+} signals. Model predicts that reduced off-rate in the whole troponin complex (TnC, TnI, TnT) versus reconstructed thin filaments (Tn, Tm, actin) alters cytosolic Ca^{2+} dynamics under control conditions or in disease-linked TnC mutations. The ultimate goal of these studies is to develop scalable methods and theories for the integration of molecular-scale information into simulations of cellular-scale systems.

Contents

1. Introduction **2**
2. Methods and software **3**
2.1. Time-dependent Smoluchowski equation 3
2.2. Reaction-diffusion equations 3
2.3. Numerical algorithms, software and meshing tools 4
3. Results and discussion **4**
3.1. Continuum diffusion on the molecular level 4
3.2. Continuum diffusion on sub-cellular level 5
4. Conclusions **11**
Acknowledgments **11**
Appendix **11**
References **12**

1. Introduction

Diffusion of enzymes and ions plays an important role in a variety of biological processes and has been studied extensively using various biophysical, biochemical and computational approaches. Computational models of diffusion have been widely used in both discrete [1] and continuum methods [2]. Discrete methods describe the stochastic trajectories of individual particles and include methods such as Monte Carlo [3], Brownian dynamics [4] and Langevin dynamics [5]. Continuum approaches model particle diffusion by the evolution of continuous probability distributions and include the Smolochowski and Fokker–Planck formalisms. Relative to discrete methods, continuum approaches provide an inexpensive alternative for the modeling of individual Brownian particles.

In our previous work, we applied adaptive finite-element methods to solve the time-dependent Smoluchowski equation on a single enzyme molecule (mouse acetylcholinesterase (mAChE)) or clusters of mAChEs [6–8]. We observed both steady-state and time-dependent diffusive particle distributions on the diffusion domain and calculated the rate association coefficient for acetylcholine (ACh) diffusive particles. Including the electrostatic field determined by solution of the Poisson–Boltzmann equation allowed us to examine the role of electrostatics in guiding diffusive particles to the active center. This study resulted in the SMOL software package, which facilitates the finite-element solution of steady-state and time-dependent Smoluchowski equations for molecular species.

Recently, the SMOL package was generalized to model signaling transduction processes on the sub-cellular level and specifically the role of calcium (Ca^{2+}) diffusion and binding to mobile and stationary buffers during the cardiac excitation–contraction cycle [9–11]. Previous approaches employed a systems biology approach, in which components of the myocyte are represented by simple geometries [12–14]. In recent years, advancements in the electron microscopy community have enabled the three-dimensional (3D) structure determination of cells and sub-cellular organelles across a wide range of spatial scales [15]. Simulations utilizing experimentally derived structures offer a degree of realism that cannot be easily captured with reduced representations.

The extended simulation tool SMOL represents progress toward unifying molecular-level and cellular-level dynamics via the solution of partial differential equations on 3D tetrahedral meshes representative of realistic systems. In this paper, we summarize the capabilities of SMOL in modeling molecular-level and cellular-level events, provide new data for myocyte cellular modeling and discuss potential further applications and extensions of the SMOL multi-scale modeling tool.

2. Methods and software

2.1. Time-dependent Smoluchowski equation

The starting point for solving the time-dependent SMOL equation is based on the steady-state Smoluchowski equation solver described by Song *et al* [16, 17]. The original time-dependent Smoluchowski equation has the form of a continuity equation,

$$\frac{\mathrm{d}u(\vec{R};t)}{\mathrm{d}t} = -\vec{\nabla}\cdot\vec{j}(\vec{R};t), \tag{1}$$

where the particle flux $\vec{j}(\vec{R};t)$ is defined as

$$\begin{aligned}\vec{j}(\vec{R};t) &= D(\vec{R})\left[\vec{\nabla}u(\vec{R};t) + \beta\vec{\nabla}W(\vec{R})u(\vec{R};t)\right]\\ &= D(\vec{R})\,\mathrm{e}^{-\beta W(\vec{R})}\nabla\mathrm{e}^{\beta W(\vec{R})}u(\vec{R};t).\end{aligned} \tag{2}$$

Here $u(\vec{R};t)$ is the distribution function of the ensemble of Brownian particles, $D(\vec{R})$ is the diffusion coefficient, $\beta = 1/k_{\mathrm{B}}T$ is the inverse Boltzmann energy, k_{B} is the Boltzmann constant, T is the temperature and $W(\vec{R})$ is the potential of mean force (PMF) for a diffusing particle due to solvent-mediated interactions with the target molecule. For simplicity, $D(\vec{R})$ is assumed constant. The two terms contributing to the flux have clear physical meaning. The first is due to free diffusion processes, as quantified by Fick's first law. The second contribution is due to the drift velocity, $\nabla W(r)/\gamma$, induced by the systematic forces, $\nabla W(r)$, and friction quantified by the friction constant γ. The relation between the diffusion coefficient $D(\vec{R})$ and the friction constant γ is given by the Stokes–Einstein equation $D\beta\gamma = 1$.

The diffusion-determined reaction rate constant during the simulation time can be obtained from the flux $\vec{j}(\vec{R};t)$ by integration over the active site boundary (Γ), i.e.

$$k_{\mathrm{on}}(t) = u_{\mathrm{bulk}}^{-1}\int_{\Gamma} n(\vec{R})\cdot j(\vec{R};t)\,\mathrm{d}S, \tag{3}$$

where u_{bulk} is the bulk concentration at the outer boundary and $n(\vec{R})$ is the surface normal [6]. The variation of reaction rates with ionic strength is often interpreted via the Debye–Huckel limiting law [18, 19].

For molecular simulations, the long-range contributions to the PMF are electrostatic in nature and thus may be estimated by solving the Poisson–Boltzmann equation. Typical approaches consider the positions of atoms from high-resolution x-ray crystal structures available in the Protein Data Bank (http://www.rcsb.org) and their corresponding partial charges, as well as the dielectric constant of the surrounding solvent. For subcellular systems, we assume that the electrostatic potential arising from the cell membrane is screened beyond the characteristic Debye length, which is less than 1.0 nm at physiological ionic strengths. As such, the $W(R)$ term defined in (2) may be neglected and one arrives at Fick's law of diffusion [6].

2.2. Reaction-diffusion equations

In this section, we derive a model that describes the diffusive transport of Ca^{2+} in the presence of stationary and mobile Ca^{2+} buffers. Assuming mass action kinetics and Fickian diffusion [20], we can write the transport equations,

$$\frac{\partial[\mathrm{Ca}^{2+}]_{\mathrm{i}}}{\partial t} = D_{\mathrm{Ca}}\nabla^2[\mathrm{Ca}^{2+}]_{\mathrm{i}} - \sum_{m=1}^{m_{\max}} R_{B_{\mathrm{m}}} - \sum_{s=1}^{s_{\max}} R_{B_{\mathrm{s}}} + J_{\mathrm{Ca_{flux}}}, \tag{4}$$

$$\frac{\partial[\mathrm{Ca}B_{\mathrm{m}}]}{\partial t} = D_{\mathrm{Ca}B_{\mathrm{m}}}\nabla^2[\mathrm{Ca}B_{\mathrm{m}}] + R_{B_{\mathrm{m}}}, \tag{5}$$

$$\frac{\partial[\mathrm{Ca}B_\mathrm{s}]}{\partial t} = R_{B_\mathrm{s}}, \tag{6}$$

$$R_{B_\mathrm{m}} = k^\mathrm{m}_\mathrm{on}([B_\mathrm{m}] - [\mathrm{Ca}B_\mathrm{m}])[\mathrm{Ca}^{2+}]_\mathrm{i} - k^\mathrm{m}_\mathrm{off}[\mathrm{Ca}B_\mathrm{m}], \tag{7}$$

$$R_{B_\mathrm{s}} = k^\mathrm{s}_\mathrm{on}([B_\mathrm{s}] - [\mathrm{Ca}B_\mathrm{s}])[\mathrm{Ca}^{2+}]_\mathrm{i} - k^\mathrm{s}_\mathrm{off}[\mathrm{Ca}B_\mathrm{s}], \tag{8}$$

where $[\mathrm{Ca}^{2+}]_\mathrm{i}$ is intracellular Ca^{2+} concentration, k^i_on and k^i_off are the association and dissociation buffer rate constants, $[B_\mathrm{s}]$ is the concentration of stationary buffer, $[B_\mathrm{m}]$ is the concentration of mobile buffer, D_Ca and $D_{\mathrm{Ca}B_\mathrm{m}}$ are the diffusion constants for free Ca^{2+} and Ca^{2+} bound to mobile buffer, and $J_{\mathrm{Ca}_\mathrm{flux}}$ is the total Ca^{2+} flux via the cell membrane.

2.3. Numerical algorithms, software and meshing tools

In 3D finite-element methods, the geometry is discretized into polyhedrons, over which the local solution to the partial differential equations may be estimated. This process is usually referred to as mesh generation [21, 22]. Although different types of meshes may be generated depending on the numerical solvers to be employed, we restrict ourselves to triangular (surface) and tetrahedral (volumetric) mesh generation as commonly used in biomedical simulation (http://fetk.org/codes/gamer/index.html). Of particular interest are 3D scalar volumes obtained by imaging techniques such as the 3D electron tomography (cellular level) and x-ray crystal structures (molecular level).

The time-dependent Smoluchowski equation and nonlinear reaction-diffusion system were solved by a finite-difference method in time and a finite-element method in space using our SMOL software tool. The SMOL program utilizes libraries from the finite-element tool kit (FEtK; http://FETK.org), which previously has been used in several molecular level studies [6–8, 23–25]. To extend SMOL to sub-cellular simulations, the reaction terms due to buffering were decoupled from the diffusion and flux boundary conditions defined in (4)–(8). Simulation results were visualized using OpenDX and GMV mesh viewers, whereas post-processing and data analyses were implemented by customized Python, MATLAB 2008b (MathWorks, Natick, MA) scripts and Xmgrace software [26].

3. Results and discussion

3.1. Continuum diffusion on the molecular level

This section demonstrates SMOL's proficiency in the numerical modeling of diffusion-limited binding kinetics of a single enzyme molecule (in this particular case, mAChE) under various ionic strength conditions [6, 19]. Acetylcholinesterase is an enzyme that hydrolyzes ACh during neuron signaling. Under physiological conditions, the experimentally suggested association rate constant (k_on) is $\sim 10^{12}\,\mathrm{M}^{-1}\,\mathrm{min}^{-1}$, which is close to the diffusion limit. Therefore, it is not easy to accurately measure k_on. By numerically solving the Poisson–Boltzmann and time-dependent Smoluchowski equations, we calculated k_on under the influence of a molecular electrostatic field. The tetrahedral mashes in this numerical experiment were obtained from the inflated van der Waals-based accessibility data for the mAChE monomer and tetramers using the level-set boundary interior exterior-mesher (figure 1) [6].

The steady-state k_on value ($t > 10\,\mu\mathrm{s}$) for a charged ligand in a 0.0 M ionic strength solution was estimated to be $9.56 \times 10^{11}\,\mathrm{M}^{-1}\,\mathrm{min}^{-1}$, which is consistent with the experimentally suggested value of $9.8 \pm 0.6 \times 10^{11}\,\mathrm{M}^{-1}\,\mathrm{min}^{-1}$ [18] and the predicted value from the time-independent solution of the Smoluchowski equation [16]. Our model studies also indicate that the mAChE association rate was rapidly attenuated by increasing the ionic strength (ranging in this numerical experiment from 0.0 to 0.67 M), which supports the idea of electrostatically guided molecular diffusion [6]. We concluded that accurate estimation of the electrostatic potential and of the time to reach steady state are important factors in modeling the activity of enzymes and buffers in cellular volumes.

To further test the SMOL solver, recently we also applied it to study the drug molecular diffusion in wild-type neuraminidase and its mutants [27]. We observed quantitatively consistent trends compared with

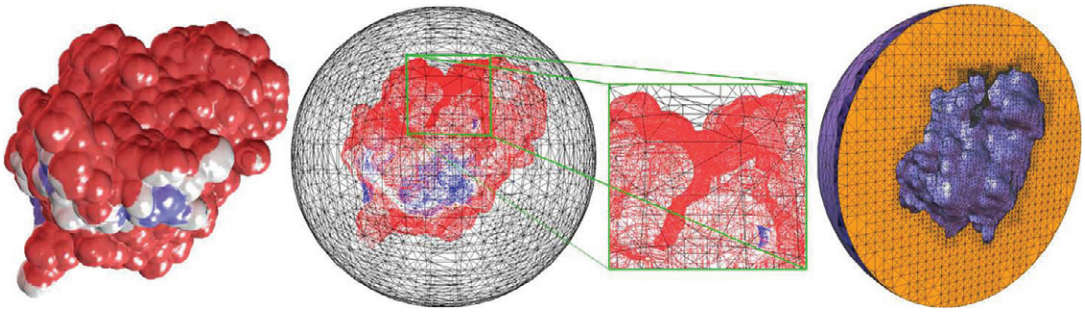

Figure 1. Left to right: mAChE monomer; the molecular surface and outer sphere; magnification of the active site gorge; the tetrahedral mesh of the internal volume between the molecular surface and the outer sphere.

experimental measurements, although the predictions were an order of magnitude higher than experiment. This indicates that the finite size of the drug molecule, as well the conformational changes of the active site of the target protein, may be significant. These attributes are neglected in the current SMOL tool. To overcome this limitation, we are developing a new multi-scale algorithm to couple the SMOL continuum formulation with particle-based Brownian dynamics. The simulation of explicit particles naturally accommodates finite-size and conformational effects that may influence association rate constants. These studies also lay the foundation for integrating molecular-scale information into cellular-scale systems such as Ca^{2+} signaling transduction in cardiac myocytes [9–11].

3.2. Continuum diffusion on sub-cellular level

In cardiac muscle cells, calcium (Ca^{2+}) is best known for its role in contraction activation [28]. A remarkable number of quantitative data on cardiac cell structure, ion-transporting protein function and distribution and intracellular Ca^{2+} dynamics have become available [15, 28–30]. Alterations in myocyte ultra-structure and in protein function and distribution are now recognized to be the primary mechanisms of cardiac dysfunction in a diverse range of common pathologies including cardiac arrhythmias and hypertrophy [28].

3.2.1. Cardiomyocyte ionic model with realistic t-tubule geometry. In this paper, we used our published computational model with realistic transverse-axial *t*-tubule geometry and experimentally suggested ion-transporting protein distributions, to analyze several important spatial and temporal features of Ca^{2+} signaling, buffering and diffusion in rat ventricular myocytes [11]. We considered a small compartment containing a single *t*-tubule and its surrounding half-sarcomeres (figure 2, middle panel). The *t*-tubule diameter varied from 0.19 to 0.469 μm and the *t*-tubule depth was 5.645 μm. The surrounding half-sarcomeres were modeled as a rectangular-shaped box of 2 μm $\times$ 2 μm in the plane of external sarcolemma and 5.96 μm in depth. Because the original *t*-tubule model did not include the realistic cell surface, one of the box faces (top red surface in figure 2) was assumed to be the external cell membrane [11]. To generate the high-fidelity and -quality tetrahedral meshes for a 3D *t*-tubular system, we used GAMer [22].

The overall scheme of the ionic model is shown in figure 2 (right panel). In this study, we examined Ca^{2+} diffusion in rat cells that were treated with ryanodine and thapsigargin to eliminate the release and uptake of Ca^{2+} by the sarcoplasmic reticulum (e.g. Ca^{2+} fluxes via the ryanodine receptors and the SR Ca^{2+} pumps blocked) [11]. At rest, Ca^{2+} influx via Ca^{2+} leak was adjusted to match Ca^{2+} efflux via NCX; thus no net movement across the cell membrane would occur. The depolarization of the sarcolemma activates L-type Ca^{2+} channels. The subsequent influx of Ca^{2+} increases the intracellular Ca^{2+} concentration ($[Ca^{2+}]_i$). Free Ca^{2+} diffuse and react throughout the cytoplasm. The equations describing Ca^{2+} fluxes via the *t*-tubule and surface membrane ($J_{Ca_{flux}} = J_{Ca} + J_{NCX} + J_{M\text{-}leak}$, where J_{Ca} is LCC Ca^{2+} influx, J_{NCX} is NCX Ca^{2+} flux and $J_{M\text{-}leak}$ is membrane Ca^{2+} leak) were the same as those in Cheng *et al* (see also appendix). The generalized SMOL package was used to solve the nonlinear reaction-diffusion system defined in (4)–(8) [11]. Unless specified

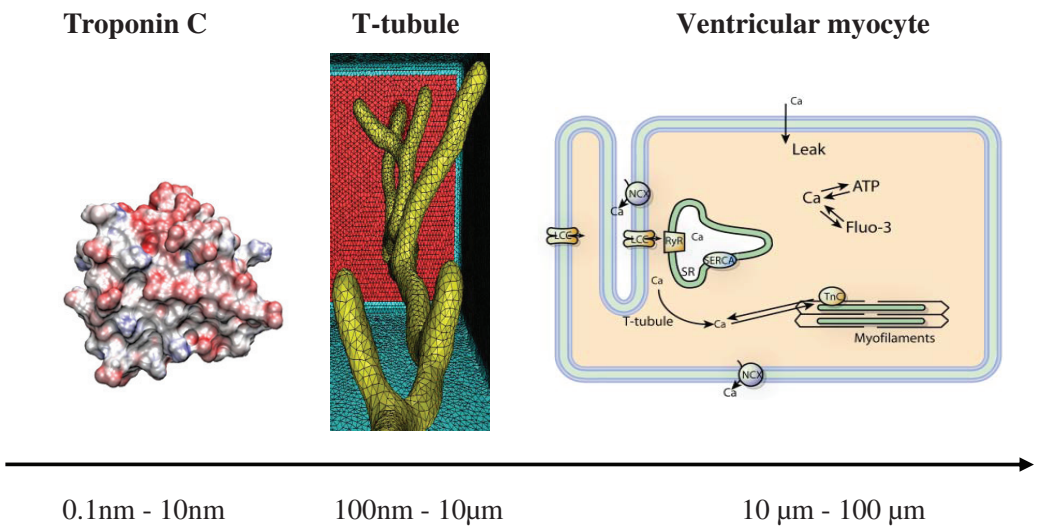

Figure 2. Left panel: troponin C monomer. Middle panel: geometric model of a single *t*-tubule and surrounding half-sarcomeres extracted from two-photon microscopy images in mice [15]. Right panel: schematic drawing of Ca^{2+} entrance and extrusion via the cell membrane and Ca^{2+} buffering and diffusion inside the cell. L-type Ca^{2+} channel (LCC), Na^{+}/Ca^{2+} exchanger (NCX), membrane Ca^{2+} leak (Leak), ryanodine receptor (RyR), sarcoplasmic reticulum (SR), SR Ca^{2+} pump (SERCA), troponin C (TnC), adenosine triphosphate (ATP) and fluorescent indicator (Fluo-3). Bottom panel*:* scale bar showing the relative lengths of the TnC macro-molecule, *t*-tubule and myocyte.

otherwise in the figure legends or in the text, all initial conditions and values of the parameters that are not included in this paper correspond to those used in Cheng *et al* [11].

In agreement with experiment [31], the model predicts that spatially uniform Ca^{2+} transients can be achieved with 100 μM Fluo-3 when total Ca^{2+} flux ($J_{Ca_{flux}}$) was heterogeneously distributed along the sarcolemma (figure 3). Figure 3 also shows that strongly non-uniform Ca^{2+} signals are predicted in the absence of a fluorescent indicator. The surface plots in figure 3 were computed from Cheng *et al* line-scan images (figures 4(F) and 6(F)) in Cheng *et al* [11]). To delineate further the suggested spatial differences in $[Ca^{2+}]_i$ (see figures 3(A) and (B)), we introduced a quantity called 'spatial Ca^{2+} heterogeneity' (SCH). The SCH is defined to be the difference of the maximal and minimal $[Ca^{2+}]_i$ values, normalized by the maximal value at a given reference point along the scanning line in a given moment t_j of interest. High SCH value suggests non-uniform $[Ca^{2+}]_i$ distribution and an SCH of zero indicates spatially uniform $[Ca^{2+}]_i$ distribution. The histogram in figure 3(C) shows that in the absence of dye, SCH (10 ms) increased by 1.64-fold, SCH (70 ms) by 2.63-fold, SCH (76 ms) by 2.68-fold, SCH (100 ms) by 4.46-fold and SCH (200 ms) by 28.65-fold.

In this particular model, the effects of exogenous and endogenous Ca^{2+} buffers (Fluo-3, ATP and troponin C) were considered. The buffer Ca^{2+} dissociation constants ($K_D^{CaFluo} = 0.739\,\mu$M, $K_D^{CaATP} = 200\,\mu$M and $K_D^{CaTn} = 1\,\mu$M) and on-rate constants $k_{on}^{CaFluo} = 0.23\,\mu M^{-1}\,ms^{-1}$, $k_{on}^{CaATP} = 0.225\,\mu M^{-1}\,ms^{-1}$ and $k_{on}^{CaTn} = 0.04\,\mu M^{-1}\,ms^{-1}$) used here are average values measured in different cardiac species under physiological conditions [9–11]. Theoretical estimates of k_{on}^{CaTn}, k_{on}^{CaATP} or k_{on}^{CaFluo} rates in the literature, however, are lacking. Moreover, the Ca^{2+}-binding buffer constants for several other important buffers regulating cardiac cell cycle (including calmodulin, myosin, TnC high-affinity sites and ADP) are controversial or unknown [12, 28]. Thus, in the event that the association rate (k_{on}) is unknown, we assume a typical near-diffusion-limited on-rate value of $0.125\,\mu M^{-1}\,ms^{-1}$ [12]. Hence, the computational estimation of these kinetic parameters presents an exciting opportunity to leverage our advanced molecular-level tools.

Two classes of Ca^{2+}-binding sites have been identified on cardiac TnC subunit (figure 2, left panel): one low-affinity Ca^{2+}-specific site on the amino end of TnC (N-domain) and two high-affinity Ca^{2+}/Mg^{2+} binding sites on the carboxy end of TnC (C-domain) [28, 32]. The high-affinity Ca^{2+}/Mg^{2+} sites are saturated at resting $[Ca^{2+}]_i$ ($\sim$100 nM). Therefore, in our model only the low-affinity Ca^{2+}-specific site was included since large and rapid changes in the Ca^{2+} occupancy of these sites can occur during the Ca^{2+} transient [32]. We assume

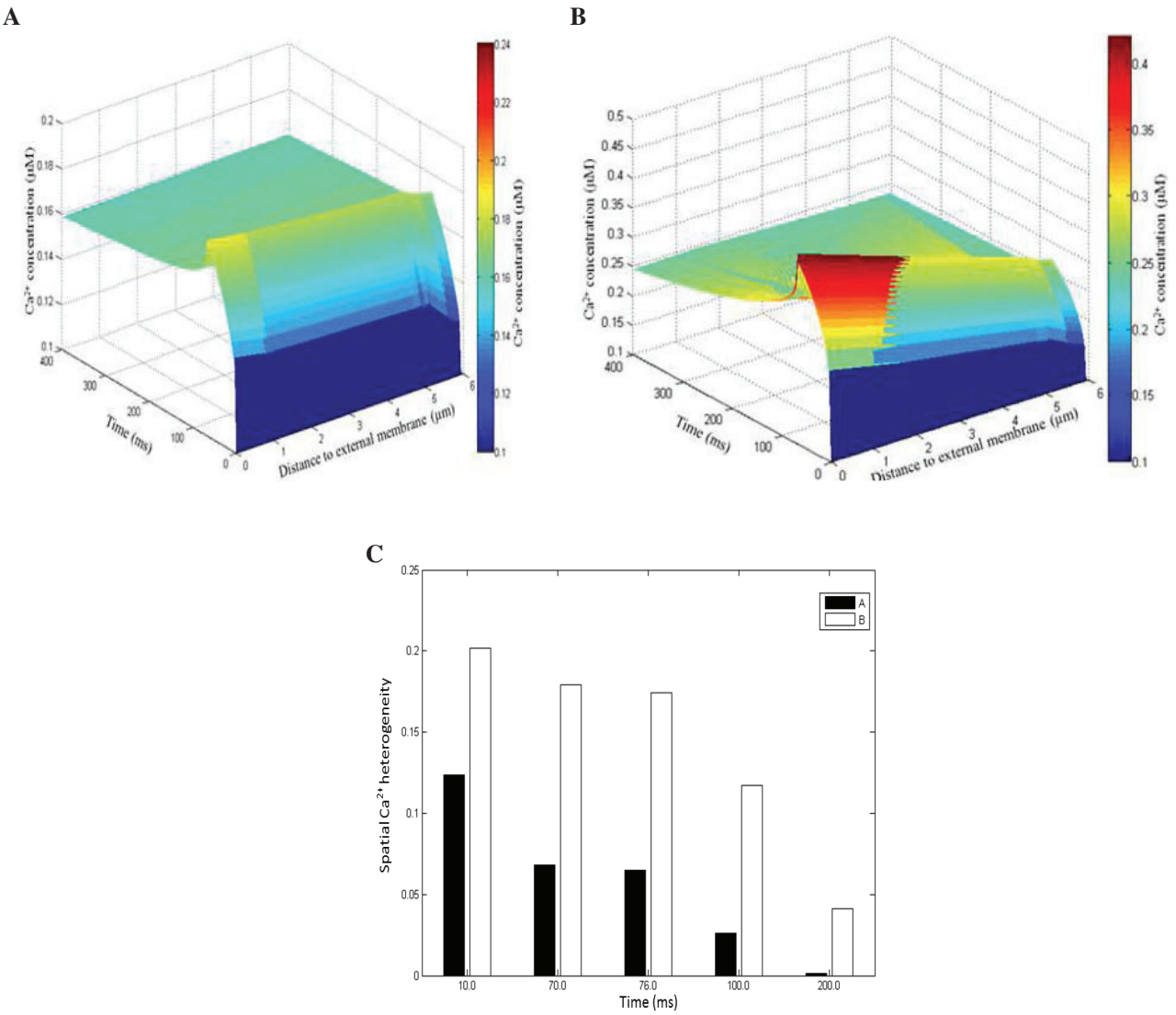

Figure 3. Ca^{2+} signals in the presence (A) and absence of dye (B). Estimated SCH with 100 μM Fluo-3 and zero Fluo-3 (C). In (A) and (B), the line scan was positioned at 200 nm from the surface of the t-tubule. Featured spots along the scanning line: 17, 3.09 and 5.45 μm. Moments t_j of interest: 10 ms—L-type Ca^{2+} current peak ($t_{I_{Ca}\text{-peak}}$); 70 ms—duration of L-type Ca^{2+} current ($t_{I_{Ca}\text{-max}}$); 76 ms—$[Ca^{2+}]_i$ peak ($t_{[Ca^{2+}]_i\text{-peak}}$); 100 and 200 ms—relaxation times for $[Ca^{2+}]_i$ ($t_{100\,ms}$, $t_{200\,ms}$).

also that TnC is immobile because it is attached to the thin filament [28]. Little is known, however, about how alterations in TnC on- and off-rates in the whole Tn compex (TnC, TnI, TnT) modulate the spatial and temporal features of the Ca^{2+} signaling, buffering and diffusion in rats. Therefore, our goal here was to examine these effects from a modeling perspective. In this study, we used published experimental measurements for k_{on}^{CaTn} and k_{off}^{CaTn} because currently at the molecular scale we do not yet have theoretical estimates as in the case of mAChE monomer on-rate [6].

3.2.1.1 Effects of changes in Ca^{2+} on-rate for TnC in the whole Tn complex on local Ca^{2+} signals. A recent study has clarified the role of a specific, disease-associated mutation of the TnC regulatory domain in altered Ca^{2+} binding, signal transmission and myocyte contractile dysfunction in rats [33]. Lim and collaborators, by combining targeted expression/integration of recombinant mutant TnC in cardiomyocytes and *in vitro* functional analysis, found a decrease in myofilament Ca^{2+} sensitivity and Ca^{2+} binding affinity. It is difficult, however, to derive from the Lim *et al* studies an understanding of how changes in the Ca^{2+} on-rate for TnC (k_{on}^{CaTnC}) modulate spatial Ca^{2+} distribution in rats. Our studies imply that in the absence of dye with 70 μM

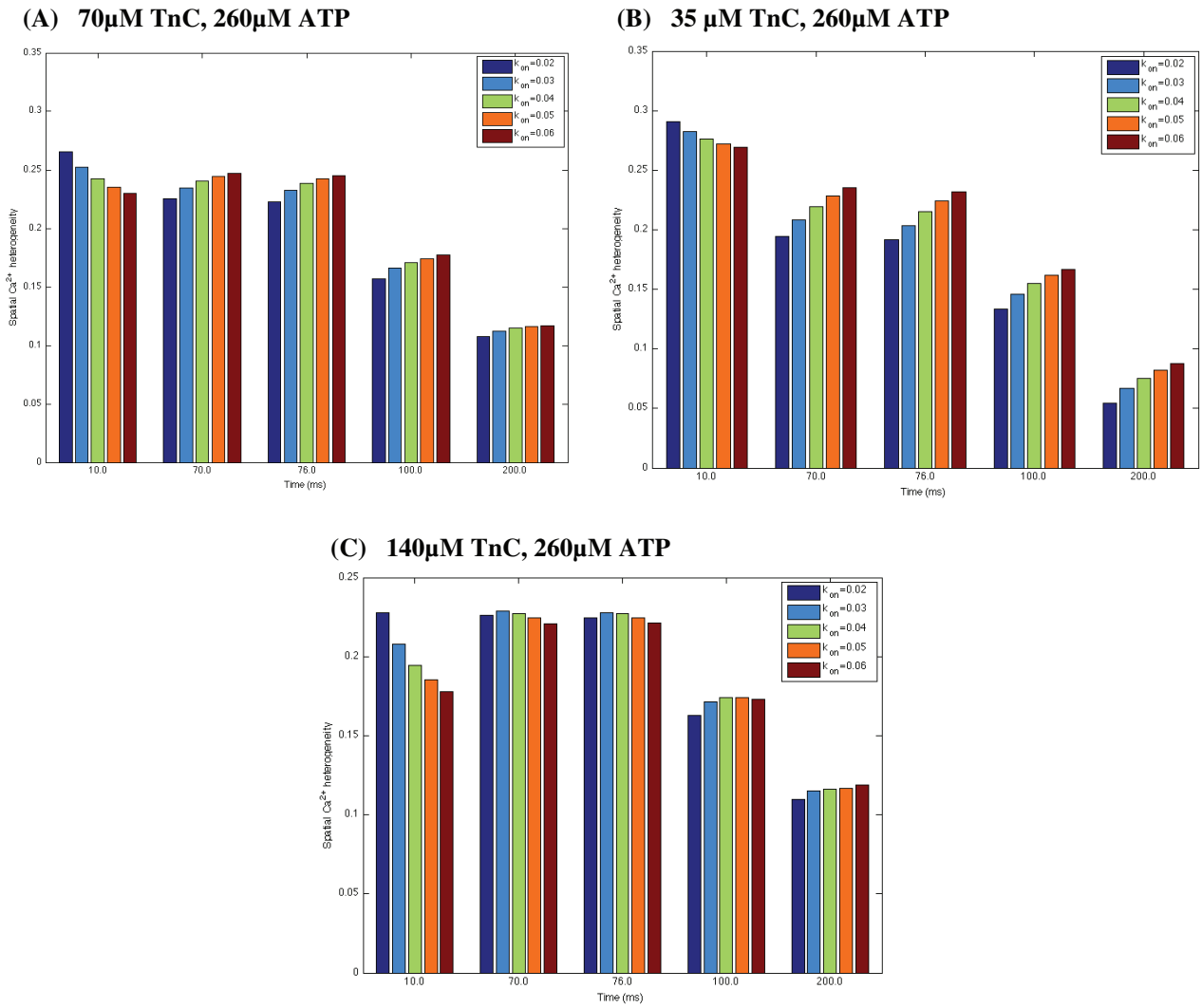

Figure 4. (A–C) Estimated spatial Ca^{2+} heterogeneity index with respect to ±25% and ±50% changes in control Ca^{2+} on-rate for TnC ($k_{on}^{CaTn} = 0.04\,\mu M^{-1}\,ms^{-1}$, assuming the basic k_{off}^{CaTn} value of $0.04\,ms^{-1}$ is unchanged) in the absence of dye. In panels (A)–(C), Ca^{2+} flux was heterogeneously distributed, line scan positioned at 200 nm away from the *t*-tubule membrane and the featured spots along the scan line were chosen to be the same as in figure 3.

TnC (see figure 4(A)), inflated k_{on}^{CaTn} values tend to decrease SCH within the initial 10 ms of simulation, during which the calcium concentration ($[Ca^{2+}]_i$) is low. SCH, however, increases at the total $[Ca^{2+}]_i$ beyond 10 ms.

Measurements have demonstrated also that the total TnC concentration ($[TnC]_{tot}$) can range from 30 to 150 μM [28, 32]. With this in mind, we computed SCH decreasing or increasing $[TnC]_{tot}$. Figures 4(A)–(C) show that at $t_{I_{Ca}\text{-peak}}$ (10 ms) 35 μM $[TnC]_{tot}$ enhanced SCH, whereas 140 μM $[TnC]_{tot}$ tends to decrease SCH as predicted with 70 μM $[TnC]_{tot}$. Interestingly, with k_{on}^{CaTn} ranging from 0.02 to 0.06 $\mu M^{-1}\,ms^{-1}$: (i) beyond 10 ms $[Ca^{2+}]_i$ was more uniformly distributed with 35 μM $[TnC]_{tot}$ than was predicted for 70 μM $[TnC]_{tot}$; (ii) 140 μM $[TnC]_{tot}$ also decreased SCH (70 μM $[TnC]_{tot}$) at $t_{I_{Ca}\text{-max}}$, $t_{[Ca^{2+}]_i\text{-peak}}$ and $t_{100\,ms}$, whereas at 200 ms SCH remained almost unchanged. Additional model findings are that with 35 μM $[TnC]_{tot}$ SCH increased at the total $[Ca^{2+}]_i$ beyond 10 ms (figure 4(B)), while the changes in k_{on}^{CaTn} slightly affected the predicted SCH (70, 76, 100 and 200 ms) when control $[TnC]_{tot}$ increased 2-fold (figure 4(C)). Taken together, our numerical work and analyses suggest that the disease-linked changes in k_{on}^{CaTn} (respectively in $K_D^{CaTn} = k_{off}^{CaTn}/k_{on}^{CaTn}$) and the alterations in $[TnC]_{tot}$ level at low free $[Ca^{2+}]_i$ (SR activity disabled) alter the effective diffusion coefficient for free Ca^{2+} (D_{Ca}^{eff}) [8, 9]. The changes in D_{Ca}^{eff} will affect local flow rates of membrane Ca^{2+} transporters and local Ca^{2+} trigger fluxes ($d[Ca^{2+}]_i/dt$) controlling SR Ca^{2+} release and ultimately the normal myocyte function [33].

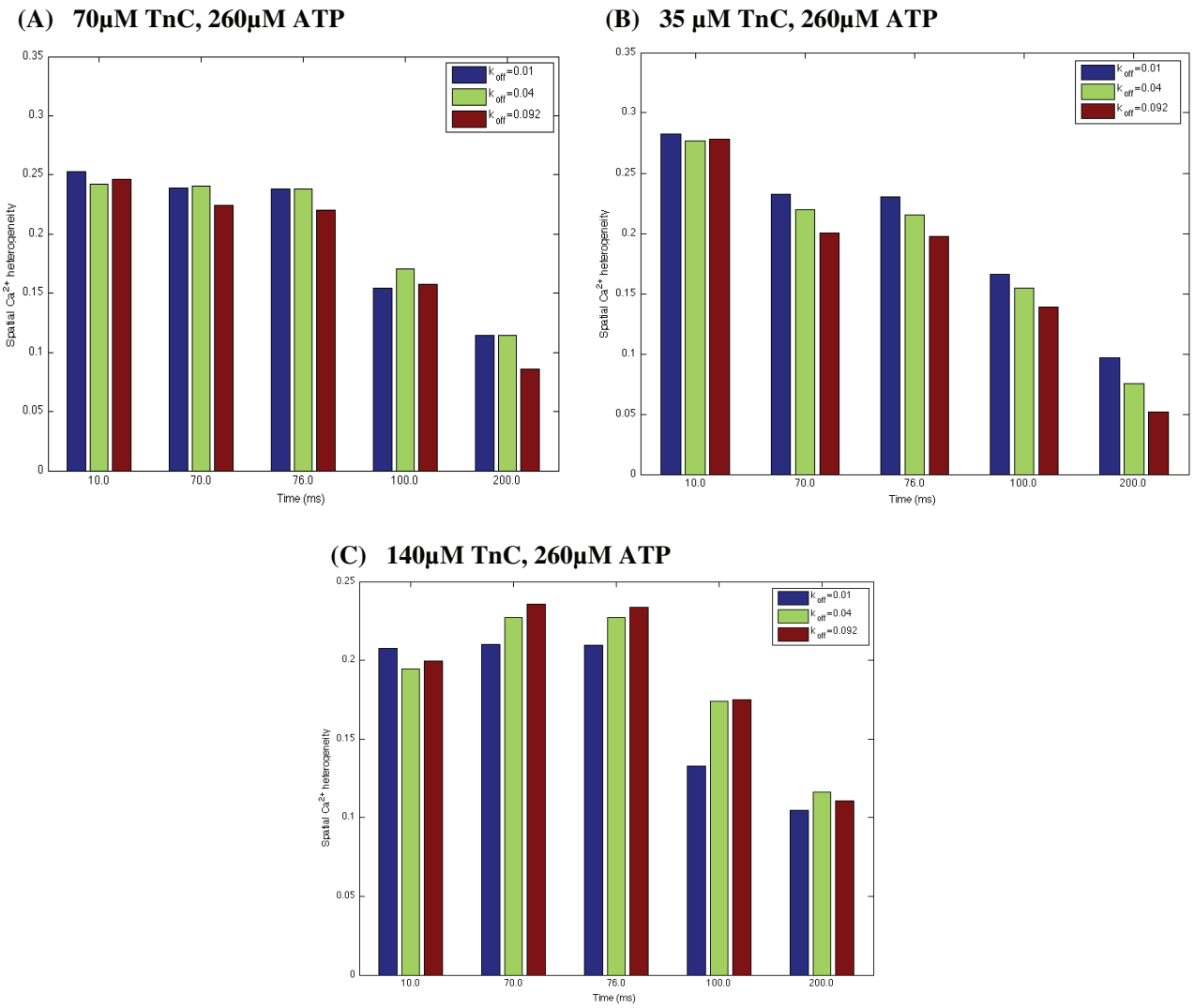

Figure 5. (A–C) Estimated spatial Ca^{2+} heterogeneity index with respect to 75% decrease and 2.3-fold increase in WT Tn off-rate ($k_{off}^{CaTn} = 0.04\,ms^{-1}$, assuming the basic k_{on}^{CaTn} value of $0.04\,\mu M^{-1}\,ms^{-1}$ is unchanged) in the absence of dye. L48Q Tn mutation—$k_{off(L48Q)}^{CaTn} 0.01\,ms^{-1}$. I61Q Tn mutation—$k_{off(I61Q)}^{CaTn} = 0.092\,ms^{-1}$. In these sets of simulations the line scan was positioned at 200 nm away from the surface of the *t*-tubule, Ca^{2+} flux was heterogeneously distributed and the reference points were chosen to be the same as in figure 3.

3.2.1.2 Effects of changes in Ca^{2+} off-rate for TnC in whole Tn complex on local Ca^{2+} signals. Kreutziger and colleagues introduced site-directed mutations in the N-terminus of rat TnC (L48Q TnC, I61Q TnC) that altered the control Ca^{2+} off-rate value [34]. Using stopped-flow spectroscopy, they measured Ca^{2+} dissociation rates from the whole troponin complex containing recombinant WT TnI and WT TnT and any one among WT TnC, L48Q TnC and I61Q TnC (in the paper, Ca^{2+} off-rates are denoted as k_{off}^{CaTn}, $k_{off(L48Q)}^{CaTn}$ or $k_{off(I61Q)}^{CaTn}$, respectively). These experiments demonstrated that the mutations in TnC altered the basic k_{off}^{CaTn} value, reducing it by 75% for L48Q TnC and increasing it by 3.2-fold for I61Q TnC. It is difficult, however, to derive from these studies an understanding of how these site-directed mutations in TnC (e.g. altered k_{off}^{CaTn}, K_D^{CaTn} and D_{Ca}^{eff}) modulate the cytosolic Ca^{2+} dynamics that ultimately will affect the normal cell function. Here, we used our 3D reaction-diffusion model to investigate this. Figure 5(A) shows that with 70 μM $[TnC]_{tot}$: (i) both the alterations in k_{off}^{CaTn} enhanced SCH at $t_{I_{Ca}\text{-peak}}$(10 ms); (ii) at $t_{I_{Ca}\text{-max}}$ (70 ms), $t_{[Ca^{2+}]_i\text{-peak}}$ (76 ms) and $t_{200\,ms}$ Q1

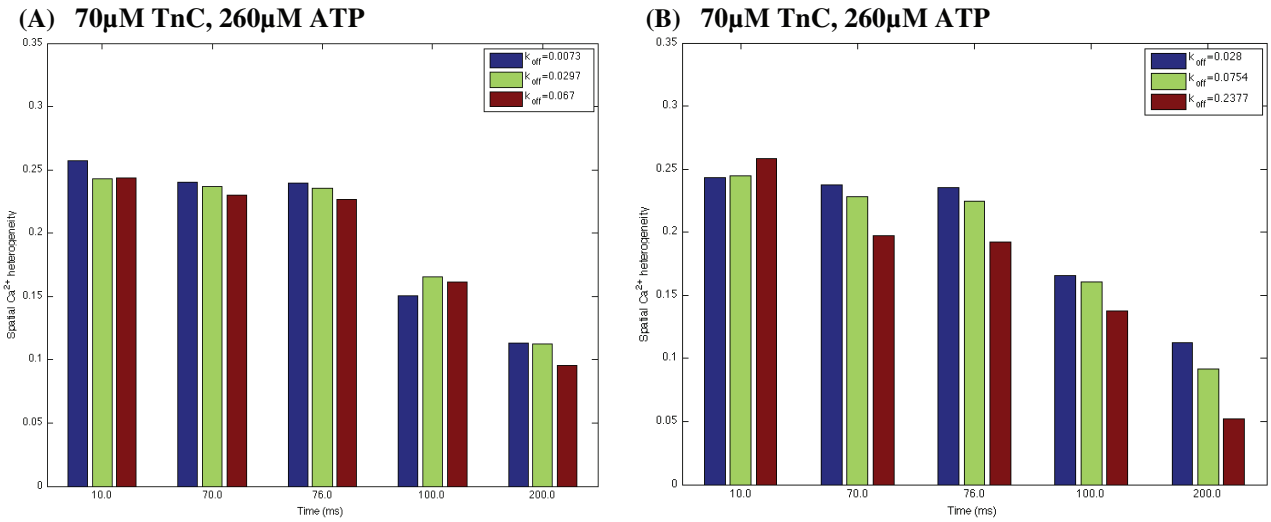

Figure 6. Estimated spatial Ca^{2+} heterogeneity index for all TnC variants in whole Tn complex (A) and reconstructed thin filaments (B) in the absence of dye. Panel (A): $k_{off}^{CaTn} = 0.0297\,ms^{-1}$, $k_{off(L48Q)}^{CaTn} = 0.0073\,ms^{-1}$ and $k_{off(I61Q)}^{CaTn} = 0.067\,ms^{-1}$. Panel (B): $k_{off}^{CaTn(TF)} = 0.0754\,ms^{-1}$, $k_{off(L48Q)}^{CaTn(TF)} = 0.028\,ms^{-1}$ and $k_{off(I61Q)}^{CaTn(TF)} = 0.2377\,ms^{-1}$. In this set of simulations: k_{on}^{CaTn} value was $0.04\,\mu M^{-1}\,ms^{-1}$; Ca^{2+} flux was heterogeneously distributed; the line scan positioned at 200 nm from the surface of the *t*-tubule; reference points along the scaned line were chosen to be the same as in figure 3.

inflated $k_{off(I61Q)}^{CaTn}$ decreased SCH, while no visible differences in SCH were found when the control k_{off}^{CaTn} was reduced by 75% (L48Q Tn mutation); (iii) at 100 ms both the alterations in k_{off}^{CaTn} decreased SCH.

The model also predicts that at $t_{I_{Ca}\text{-peak}}$ the decrease in control TnC buffer capacity to 35 μM increased SCH, whereas 140 μM $[TnC]_{tot}$ decreased SCH for all TnC variants (figures 5(A)–(C)). In addition, figure 5(B) demonstrates that with 35 μM $[TnC]_{tot}$, SCH decreased at the total $[Ca^{2+}]_i$ beyond 10 ms. The predicted changes in SCH beyond 10 ms with 140 μM $[TnC]_{tot}$ are shown in figure 5(C). This set of simulations demonstrates that: (i) at 70 and 76 ms, inflated $k_{off(I61Q)}^{CaTn}$ increased SCH, while $[Ca^{2+}]_i$ was more uniformly distributed when k_{off}^{CaTn} was decreased (L48Q Tn mutation); (ii) at 100 ms no visible differences in SCH were found when k_{off}^{CaTn} was increased 2.3-fold (I61Q Tn mutation), while a 75% drop in the basic k_{off}^{CaTn} (L48Q Tn mutation) decreased SCH notably; (iii) at 200 ms both the alterations in k_{off}^{CaTn} tended to decrease the SCH. In summary, our results demonstrate that the mutation-linked changes in k_{off}^{CaTn} (in K_D^{CaTn}, respectively) and the variations in $[TnC]_{tot}$ levels alter control D_{Ca}^{eff}, thereby altering the local sarcolemmal fluxes, SR Ca^{2+} trigger fluxes and local $[Ca^{2+}]_i$ inside the cell with SR disabled. The model also demonstrates that the alterations in k_{off}^{CaTn} may affect quite differently local Ca^{2+} distributions ($[Ca^{2+}]_i$ and $d[Ca^{2+}]_i/dt$) with respect to those when control k_{on}^{CaTn} is varied (compare figures 4 and 5).

In Kreutziger *et al*'s experiment, k_{off}^{CaTn} was determined for each Tn ($k_{off}^{CaTn} = 0.0297\,ms^{-1}$; $k_{off(L48Q)}^{CaTn} = 0.0073\,ms^{-1}$; $k_{off(I61Q)}^{CaTn} = 0.067\,ms^{-1}$) by fitting fluorescence data (at 15 °C) with exponential curves [34]. We then calculated SCH replacing the model k_{off}^{CaTn} values (0.01 ms^{-1} L48Q Tn, 0.04 ms^{-1} WT Tn and 0.092 ms^{-1} I61Q Tn) with the experimentally measured values. However, only minor effects in predicted SCH were found with 70 μM $[TnC]_{tot}$ (compare figures 5(A) and 6(A)).

3.2.1.3 Effects of changes in Ca^{2+} off-rate for TnC in reconstructed thin filaments on local Ca^{2+} signals. Recently, Kreutziger *et al* [34] measured the off-rates in reconstructed thin filaments with WT or mutant whole TnC, WT Tm and WT actin (in the paper these Ca^{2+} off-rates are denoted as $k_{off}^{CaTn(TF)}$, $k_{off(L48Q)}^{CaTn(TF)}$ or $k_{off(I61Q)}^{CaTn(TF)}$, respectively). They found 2.2–3.4-fold increases in off-rates for all TnC variants versus the isolated whole Tn complex. The relative effect of the mutations in TnC remained almost the same as for whole Tn, such that $k_{off}^{CaTn(TF)}$was reduced by 63% for L48Q (versus 75% in isolated Tn complex) and increased by 3.2-fold for I61Q Tn in the thin filaments. It remains unclear, however, whether the changes in off-rates in reconstructed

thin filaments would have a different effect on Ca^{2+} dynamics relative to those predicted with the isolated whole Tn complex. Our numerical results demonstrate that with 70 μM $[TnC]_{tot}$ visible differences in the calculated SCH values compared to those in isolated whole Tn complex were found. At I_{Ca} peak (10 ms) a ~2.5-fold increase in WT variant had little or no effect on SCH, a ~3.85-fold increase in L48Q variant decreased SCH, while a ~3.55-fold increase in I61Q variant increased SCH (figures 6(A) versus 6(B)).

Figures 5 and 6 also show that at the moment of I_{Ca} closing (70 ms) and at $[Ca^{2+}]_i$ peak (76 ms), SCH decreased for WT and I61Q variants versus the whole Tn complex. The model also predicts that: (i) at $t_{100\,ms}$ $SCH(k_{off}^{CaTn}) \sim SCH(k_{off}^{CaTn(TF)})$, $SCH(k_{off(L48Q)}^{CaTn}) < SCH(k_{off(L48Q)}^{CaTn(TF)})$ and $SCH(k_{off(I61Q)}^{CaTn}) > SCH(k_{off(I61Q)}^{CaTn(TF)})$; (ii) at $t_{200\,ms}$ $SCH(k_{off}^{CaTn}) > SCH(k_{off}^{CaTn(TF)})$, $SCH(k_{off(L48Q)}^{CaTn}) \sim SCH(k_{off(L48Q)}^{CaTn(TF)})$ and $SCH(k_{off(I61Q)}^{CaTn}) > SCH(k_{off(I61Q)}^{CaTn(TF)})$. These findings suggest that the use of whole Tn off-rates versus reconstructed thin filament off-rates into cardiac cellular and sub-cellular models may alter the predicted control and disease-linked Ca^{2+} transporter rates, Ca^{2+} trigger fluxes for SR release and local Ca^{2+} signals.

In summary, our studies provide a foundation for a more comprehensive understanding of signaling transduction at molecular and sub-cellular scales. Our studies also illustrate the importance of improved experimental measurements of Ca^{2+} buffering kinetics and of complementary theoretical estimates of Ca^{2+} buffer reaction rates. Together, this will lead to a better understanding of Ca^{2+} signaling in the heart under normal or pathological conditions. Q2

4. Conclusions

In this paper, we applied the SMOL package to molecular-level reaction kinetics of ACh and cellular-level Ca^{2+} dynamics. Our data demonstrate that a continuum-based description of ion diffusion, the Smoluchowski equation, captures molecular-level details impacting reaction rates. This suggests that alternative descriptions of electrodynamics, such as the Poisson–Nernst–Planck equation, could further improve our estimates. These data also demonstrate progress toward sub-cellular modeling of the heart, in which buffering dynamics are handled at a molecular level. Future applications of SMOL will feature spatially coupled 3D structural and functional models of ventricular cardiac myocytes with (i) realistic sub-cellular anatomical structures, such as Ca^{2+}-signaling micro-domains and cell organelles; (ii) sarcoplasmic reticulum fluxes via ryanodine receptors (RyR) and the SERCA pump; and (iii) spatial and temporal scales spanning from single-channel ion fluxes to tension development in actin and myosin filaments. These developments would facilitate modeling excitation–contraction coupling influenced by mutations, phosphorylation and alterations in protein expression. Other molecular-level approaches that could further benefit excitation–contraction modeling include analysis of nucleotide-activated conformational dynamics [35], kinase activity [36], channel gating [37] and structure-based drug design [38]. In concert, these approaches constitute a prototypical workflow for patient-specific modeling and therapies.

Acknowledgments

This work was supported by the National Biomedical Computational Resource (NIH grant no. 5P41 RR08605–17). JAMcC acknowledges additional support from NIH, NSF, Howard Hughes Medical Institute and the Center for Theoretical Biological Physics. Q3

Appendix

Equations describing total Ca^{2+} flux ($J_{Ca_{flux}}$), L-type Ca^{2+} current (J_{Ca}), Na^+/Ca^{2+} exchanger flux (J_{NCX}) and Ca^{2+} leak current ($J_{M\text{-}leak}$) throughout the *t*-tubule and external membrane:

$$J_{Ca_{flux}} = J_{Ca} + J_{NCX} + J_{M\text{-}leak}, \tag{A.1}$$

$$I_{Ca}(t) = I_{Ca_o} f(t) \tag{A.2}$$

Table 1. Membrane calcium fluxes parameters

Symbol	Definition	Value	Reference
L-type Ca^{2+} current			
I_{Ca_o}	Constant	1	[9]
t_a	Constant	4 ms	[40]
t_b	Constant	70 ms	[40]
Na^+/Ca^{2+} exchange current			
$[Na^+]_e$	Extracellular Na^+ concentration	140 mM	[28]
$[Na^+]_i$	Resting Na^+ concentration	10 mM	[28]
g_{NCX}	Pump rate of NCX	38.5 μM ms^{-1}	[41]
η	Voltage dependence of NCX control	0.35	[41]
$k_{m,Na}$	Na^+ half saturation of NCX	87.5 mM	[41]
$k_{m,Ca}$	Ca^{2+} half saturation of NCX	1380 μM	[41]
k_{sat}	Low potential saturation factor of NCX	0.1	[41]
Membrane Ca^{2+} leak			
$g_{M\text{-}leak}$	Conductance	3.4e − 6 μM mV^{-1} ms^{-1}	Estimated

$$f(t) = \begin{cases} 1.14380t, & 0 < t < t_a, \\ 1.73189 + 5.11444\,e^{-\frac{t}{30.31164}}, & t_a \leqslant t < t_b, \\ 0, & t \geqslant t_b, \end{cases} \tag{A.3}$$

$$I_{NCX} = g_{NCX} \frac{e^{\eta VF/RT}[Na^+]_i^3[Ca^{2+}]_e - e^{(\eta-1)VF/RT}[Na^+]_e^3[Ca^{2+}]_i}{(k_{m,Na}^3 + [Na^+]_e^3)(k_{m,Ca} + [Ca^{2+}]_e)(1 + k_{sat}e^{(\eta-1)VF/RT})}, \tag{A.4}$$

$$I_{M-leak} = g_{M\text{-}leak}([Ca^{2+}]_e - [Ca^{2+}]_i). \tag{A.5}$$

Flux parameter values were estimated or taken from the literature (see table 1). In this study, the Ca^{2+} leak is not actually a particular 'leak protein'. The Ca^{2+} leak was included and adjusted so that at rest Ca^{2+} influx via Ca^{2+} leak matches Ca^{2+} efflux via NCX and thus no net movement across the cell membrane occurs.

In the model, each current density (I_i) was converted to Ca^{2+} flux (J_i) by using the experimentally suggested surface to volume ratio ($\frac{C_m}{V_{cell}}$~8.8 pF/pL) in adult rat ventricular myocytes [39]:

$$J_i = \left(\frac{1}{2F}\frac{C_m}{V_{cell}}\right) I_i. \tag{A.6}$$

The voltage-clamp protocol (holding potential –50 mV; electric pulse of 10 mV for 70 ms) and whole-cell L-type Ca^{2+} current were derived from the Zahradnikova *et al* data with the blocked SR activity [40].

References

[1] Ermak D L and McCammon J A 1978 Brownian dynamics with hydrodynamic interactions *J. Chem. Phys.* **69** 1352–60

[2] Smart J L and McCammon J A 1998 Analysis of synaptic transmission in the neuromuscular junction using a continuum finite element model *Biophys. J.* **75** 1679–88

[3] Berry H 2002 Monte-Carlo simulations of enzyme reactions in two dimensions: fractal kinetics and spatial segregation *Biophys. J.* **83** 1891–901

[4] McCammon J A 1987 Computer-aided molecular design *Science* **238** 486–91

[5] Eastman P and Doniach S 1998 Multiple time step diffusive langevin dynamics for proteins *Proteins* **30** 215–27

[6] Cheng Y, Suen J K, Zhang D, Bond S D, Zhang Y, Song Y, Baker N A, Bajaj C, Holst M J and McCammon J A 2007 Finite element analysis of the time-dependent Smoluchowski equation for acetylcholinesterase reaction rate calculations *Biophys. J.* **92** 3397–406

[7] Cheng Y, Suen J K, Radić Z, Bond S D, Holst M J and McCammon J A 2007 Continuum simulations of acetylcholine diffusion with reaction-determined boundaries in neuromuscular junction models *Biophys. Chem.* **127** 129–39

[8] Cheng Y, Chang C, Yu Z, Zhang Y, Sun M, Leyh T S, Holst M J and McCammon J A 2008 Diffusional channeling in the sulfate activating complex: combined continuum modeling and coarse-grained Brownian dynamics studies *Biophys. J.* **95** 4659–67

[9] Michailova A, DelPrincipe F, Egger M and Niggli E 2002 Spatiotemporal features of Ca^{2+} signaling, buffering and diffusion in atrial myocytes with inhibited sarcoplasmic reticulum *Biophys. J.* **83** 3134–51

[10] Lu S *et al* 2009 Multi-scale modeling in rodent ventricular myocytes: contributions of structural and functional heterogeneities to excitation-contraction coupling *IEEE Eng. Med. Biol.* **28** 46–57

[11] Cheng Y, Yu Z, Hoshijima M, Holst M J, McCulloch A D, McCammon J A and Michailova A 2010 Numerical analysis of Ca^{2+} signaling in rat ventricular myocytes with realistic transverse-axial tubular geometry and inhibited sarcoplasmic reticulum *PloS Comput. Biol.* **6** e1000972

[12] Michailova A and McCulloch A D 2001 Model study of ATP and ADP buffering, transport of Ca^{2+} and Mg^{2+}, and regulation of ion pumps in ventricular myocyte *Biophys. J.* **81** 614–29

[13] Michailova A, Saucerman J, Belik M E and McCulloch A D 2005 Modeling regulation of cardiac KATP and L-type Ca^{2+} currents by ATP, ADP and Mg^{2+} *Biophys. J.* **88** 2234–49

[14] Michailova A, Lorentz W and McCulloch A D 2007 Modeling transmural heterogeneity of KATP current in rabbit ventricular myocytes *Am. J. Physiol. Cell Physiol.* **293** 542–57

[15] Hayashi T, Martone M E, Yu Z, Thor A, Doi M, Holst M J, Ellisman M E and Hoshijima M 2009 Three-dimensional electron microscopy reveals new details of membrane systems for Ca^{2+} signaling in the heart *J. Cell Sci.* **122** 1005–13

[16] Song Y, Zhang Y, Shen T, Bajaj C, McCammon J A and Baker N A 2004 Finite element solution of the steady-state Smoluchowski equation for rate constant calculations *Biophys. J.* **86** 2017–29

[17] Song Y, Zhang Y, Bajaj C and Baker N A 2004 Continuum diffusion reaction rate calculations of wild-type and mutant mouse acetylcholinesterase: adaptive finite element analysis *Biophys. J.* **87** 1558–66

[18] Radić Z, Quinn D M, McCammon J A and Taylor P 1997 Electrostatic influence on the kinetics of ligand binding to acetylcholinesterase—distinctions between active center ligands and fasciculin *J. Biol. Chem.* **272** 23265–77

[19] Quinn D M, Seravalli J H K, Medhekar N R, Husseini B, Radić Z, Vellom D C, Pickering N and Taylor P 1995 *Enzymes of the Cholinesterase Family* (New York: Plenum)

[20] Keizer J 1987 *Statistical and Thermodynamics Nonequilibrium Processes* (New York: Springer)

[21] Yu Z, Holst M J, Cheng Y and McCammon J A 2008 Feature-preserving adaptive mesh generation for molecular shape modeling and simulation *J. Mol. Graph. Model.* **26** 1370–80

[22] Yu Z, Holst M J and McCammon J A 2008 High-fidelity geometric modelling for biomedical applications *Finite Elem. Anal. Des.* **44** 715–23

[23] Bank R and Holst M J 2003 A new paradigm for parallel adaptive meshing algorithms *SIAM Rev.* **45** 291–323

[24] Holst M 2001 Adaptive numerical treatment of elliptic systems on manifold *Adv. Comput. Math.* **15** 139–91

[25] Zhang D, Suen J K, Zhang Y, Song Y, Radić Z, Taylor P, Holst M J, Bajaj C, Baker N A and McCammon J A 2005 Tetrameric mouse acetylcholinesterase: continuum diffusion rate calculations by solving the steady-state Smoluchowski equation using finite element methods *Biophys. J.* **88** 1659–65

[26] Vaught A 1996 Graphing with Gnuplot and Xmgr. *Linux J.*

[27] Cheng Y, Holst M J and McCammon J A 2009 Finite element analysis of drug electrostatic diffusion: inhibition rate studies in N1 neuraminidase *Pacific Symp. Biocomputing* **14** 281–92

[28] Bers D M 2001 *Excitation-Contraction Coupling and Cardiac Contractile Force* (Dortrecht: Kluwer)

[29] Scriven D R, Klimek A, Lee K L and Moore E W 2002 The molecular architecture of calcium microdomains in rat cardiomyocytes *Ann. New York Acad. Sci.* **976** 488–99

[30] Thomas M J, Sjaastad I, Andersen K, Helm P J, Wasserstrom J A, Sejersted O M and Ottersen O P 2003 Localization and function of the Na^{2+}/Ca^{2+}-exchanger in normal and detubulated rat cardiomyocytes *J. Mol. Cell. Cardiol.* **35** 1325–37

[31] Cheng H, Cannell M B and Lederer W J 1994 Propagation of excitation–contraction coupling into ventricular myocytes *Pflugers Arch.* **428** 415–17
[32] Robertson S P, Johnson J D and Potter J D 1981 The time-course of Ca^{2+} exchange with calmodulin, troponin, parvalbumin, and myosin in response to transient increase in *Biophys. J* **34** 559–69
[33] Lim C C *et al* 2008 A novel mutant cardaic troponin C disrupts molecular motions critical for calcium binding affinity and cardiomyocyte contractility *Biophys. J.* **94** 3577–89
[34] Kreutziger K L, Piroddi N, McMichael J T, Tesi C, Poggesi C and Regnier M 2011 Calcium binding kinetics of troponin C strongly modulate cooperative activation and tension kinetics in cardiac muscle *J. Mol. Cell. Cardiol.* **50** 165–74
[35] Grant B J, Gorfe A A and McCammon J A 2009 Ras conformational switching: simulating nucleotide-dependent conformational transitions with accelerated molecular dynamics *PLoS Comput. Biol.* **5** e1000325
[36] Khavrutskii J V, Grant B, Taylor S S and McCammon J A 2009 A transition path ensemble study reveals a linchpin role for Mg^{2+} during rate-limiting ADP release from protein kinase A *Biochemistry* **48** 11532–45
[37] Wang H-L, Toghraee R, Papke D, Cheng X-L, McCammon J A, Ravaioli U and Sine S M 2009 Single-channel current through nicotinic receptor produced by closure of binding site C-loop *Biophys. J.* **96** 3582–90
[38] Ivetac A and McCammon J A 2010 Mapping the druggable allosteric space of G-protein coupled receptors: a fragment-based molecular dynamics approach *Chem. Biol. Drug Des.* **76** 201–17
[39] Satoh H, Delbridge L M, Blatter L A and Bers D M 1996 Surface: volume relationship in cardiac myocytes studied with confocal microscopy and membrane capacitance measurements: species-dependence and developmental effects. *Biophys. J.* **70** 1494–1504
[40] Zahradnikova A, Kubalova Z, Pavelková J, Györke S and Zahradník I 2004 Activation of calcium release assessed by calcium release-induced inactivation of calcium current in rat cardiac myocytes *Am. J. Physiol. Cell Physiol.* **286** C330–41
[41] Hinch R, Greenstein J L, Tanskanen A J, Xu L and Winslow R L 2004 A simplified local control model of calcium induced calcium release in cardiac ventricular myocytes *Biophys. J.* **87** 3723–36